ACS NANO
Cite This: ACS Nano 2019, 13, 10376−10385
www.acsnano.org

ARTICLE

Ultrafast Zinc-Ion Diffusion Ability Observed in 6.0-Nanometer Spinel Nanodots

Le Jiang, Zeyi Wu, Yanan Wang, Wenchao Tian, Zhiying Yi, Cailing Cai, Yingchang Jiang, and Linfeng Hu*

Department of Materials Science, Fudan University, Shanghai 200433, People's Republic of China

Supporting Information

ABSTRACT: Rechargeable aqueous Zn-ion batteries (ZIBs) have recently attracted much attention due to their low cost and superior safety. Unfortunately, their low capacity and poor cycle life still hinder their practical application. Here, we have developed a general synthesis strategy for ultrasmall spinel oxide nanodots (Mn_3O_4, $CoMn_2O_4$, $MnCo_2O_{4.5}$, Co_3O_4, and $ZnMn_2O_4$) with abundant oxygen vacancies and highly active surface. Among them, 6.0-nanometer-sized Mn_3O_4 nanodots deliver the best Zn-ion storage ability with a high reversible capacity of 386.7 mA h g^{-1} at 0.1 A g^{-1}, excellent rate performance, and a long-term stability of 500 cycles at 0.5 A g^{-1}. Taking advantage of the highly activated surficial atoms, shortened transfer pathway, and introduction of numerous oxygen vacancies, an ultrahigh Zn^{2+} diffusion coefficient of 2.4×10^{-10} cm^2 s^{-1} has been detected during the discharge process. This value is more than 2 orders of magnitude higher than that of other spinel oxide nanostructures in previous reports and also the highest one in all of the as-reported ZIB cathode materials to date. Our finding offers promising opportunities for the development of ZIB cathode materials with high energy density, long-term cycling stability, excellent flexibility, and wearability.

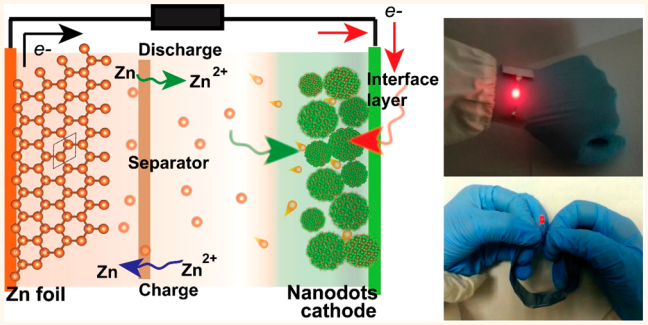

KEYWORDS: *spinel nanodots, Zn-ion battery, diffusion coefficient, active surface, flexibility*

Electrochemical energy storage devices, such as rechargeable batteries, are critical for meeting the worldwide growing demand for electrical energy.[1] In the past decades, lithium-ion batteries (LIBs), a representative type of competitive and practical battery, have been widely commercialized and applied in the whole electronic industry.[2] However, increasing concerns about limited lithium resources, high cost, and insecurity of organic electrolyte scale-up limit their further development.[3] As one of the most promising secondary battery recently, aqueous Zn-ion rechargeable batteries (ZIBs) with mild aqueous electrolyte have attracted considerable attention and global interest owing to their apparent advantages as follows: (1) low cost: the abundance of Zn is significantly higher than that of Li, leading to a much lower cost for cell fabrication; (2) nontoxicity of Zn results in better environmental friendliness; (3) the low redox potential of −0.76 V *versus* standard hydrogen electrode (SHE) leads to excellent stability in water due to a high overpotential for hydrogen evolution;[4−6] (4) superior safety: most of the as-reported ZIBs are based on an aqueous liquid electrolyte with the absence of any flammable organic component, which significantly relieves environmental contamination and improves the safety.[7,8] Unfortunately, the low capacity and poor cycle life of the present rechargeable aqueous ZIBs still hinder their practical application.[9,10]

Recent advances have successfully demonstrated the promising Zn-ion storage using spinel-structured metal oxides as a cathode.[11−19] Typically, Zhang *et al.* successfully realized rechargeable Zn-ion storage in cation-deficient spinel $ZnMn_2O_4$ nanoparticles with an average size of about 15 nm, exhibiting a reversible capacity of 150 mA h g^{-1} and a capacity retention of 94% over 500 cycles.[11] Kang *et al.* reported Mn_3O_4 as a cathode material suitable for a neutral aqueous rechargeable zinc battery with a maximum capacity of 239.2 mA h g^{-1} at a current density of 0.1 A g^{-1}.[12] Subsequently, Liang *et al.* rationally designed a Mn_3O_4/3D substrate composite as a binder-free cathode for aqueous ZIBs, delivering a higher specific capacity of 296 mA h g^{-1} at 0.1 A g^{-1}.[13] Nevertheless, the development of ZIBs using spinel oxide as cathode material is still in its infancy, and their reported electrochemical performances (capacity, cycle ability, *etc.*) have remained far from practical requirements. For example, Mn_3O_4 spinel shows a theoretical capacity of ∼468.56 mA h g^{-1} for ZIBs, and the optimized value in all previous work is only 296 mA h g^{-1}.[13]

Received: May 28, 2019
Accepted: August 5, 2019
Published: August 5, 2019

DOI: 10.1021/acsnano.9b04165
ACS Nano 2019, 13, 10376−10385

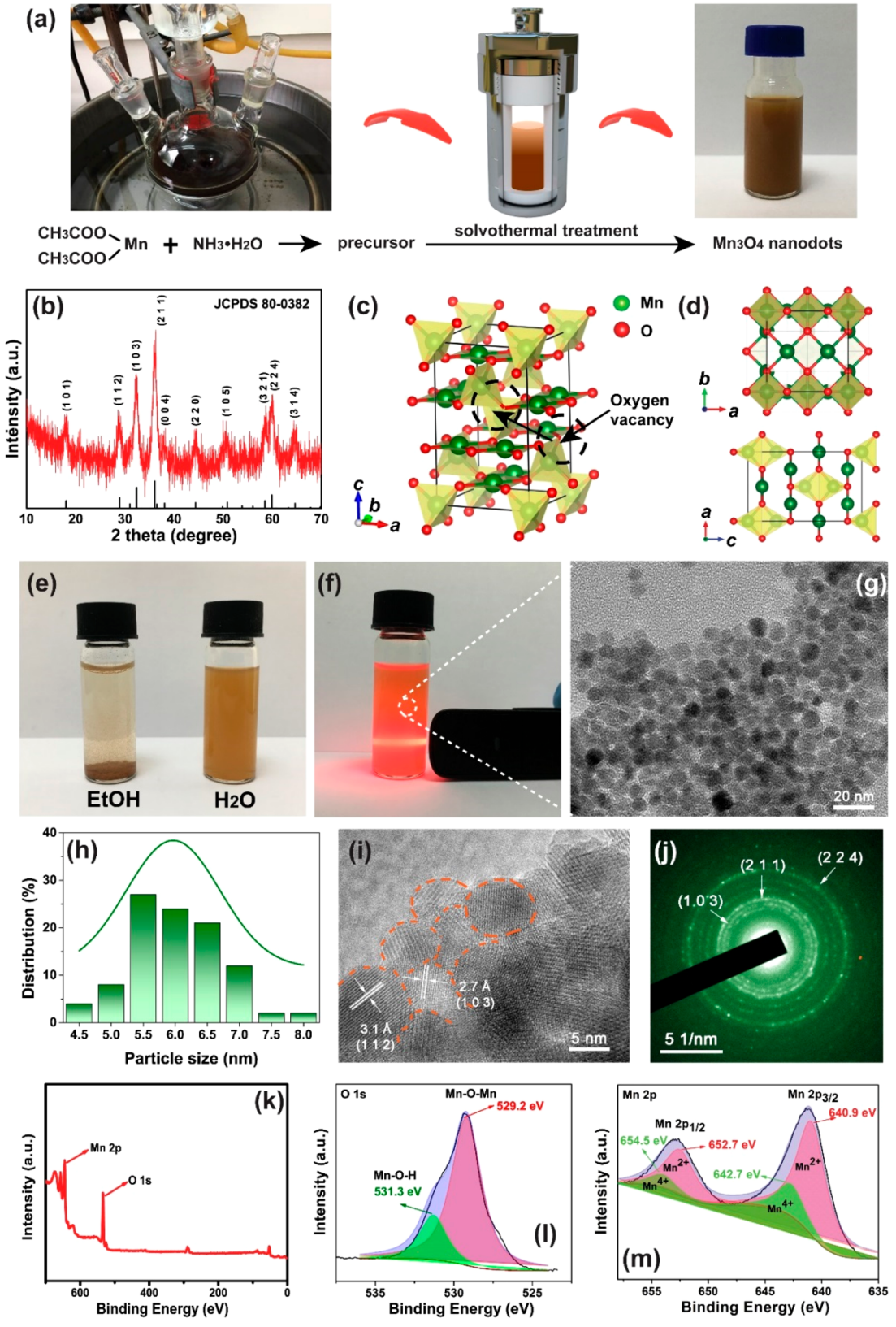

Figure 1. (a) Schematic illustration of the synthesis of Mn_3O_4 nanodots as the high-performance cathode of a rechargeable zinc ion battery. (b) Powder XRD pattern, (c) 3D crystal structure, and (d) 2D atomic configuration of as-prepared Mn_3O_4 nanodots. (e) Optical image of as-prepared Mn_3O_4 nanodots in EtOH and H_2O solvent, respectively. (f) Formation of homogeneous dispersions in H_2O solvent with a typical Tyndall effect. (g) Typical TEM of the Mn_3O_4 nanodots and (h) the corresponding size distribution. (i) HRTEM images and (j) the corresponding SAED pattern. (k) XPS survey spectrum and high-resolution (l) O 1s and (m) Mn 2p spectrum.

DOI: 10.1021/acsnano.9b04165
ACS Nano 2019, 13, 10376−10385

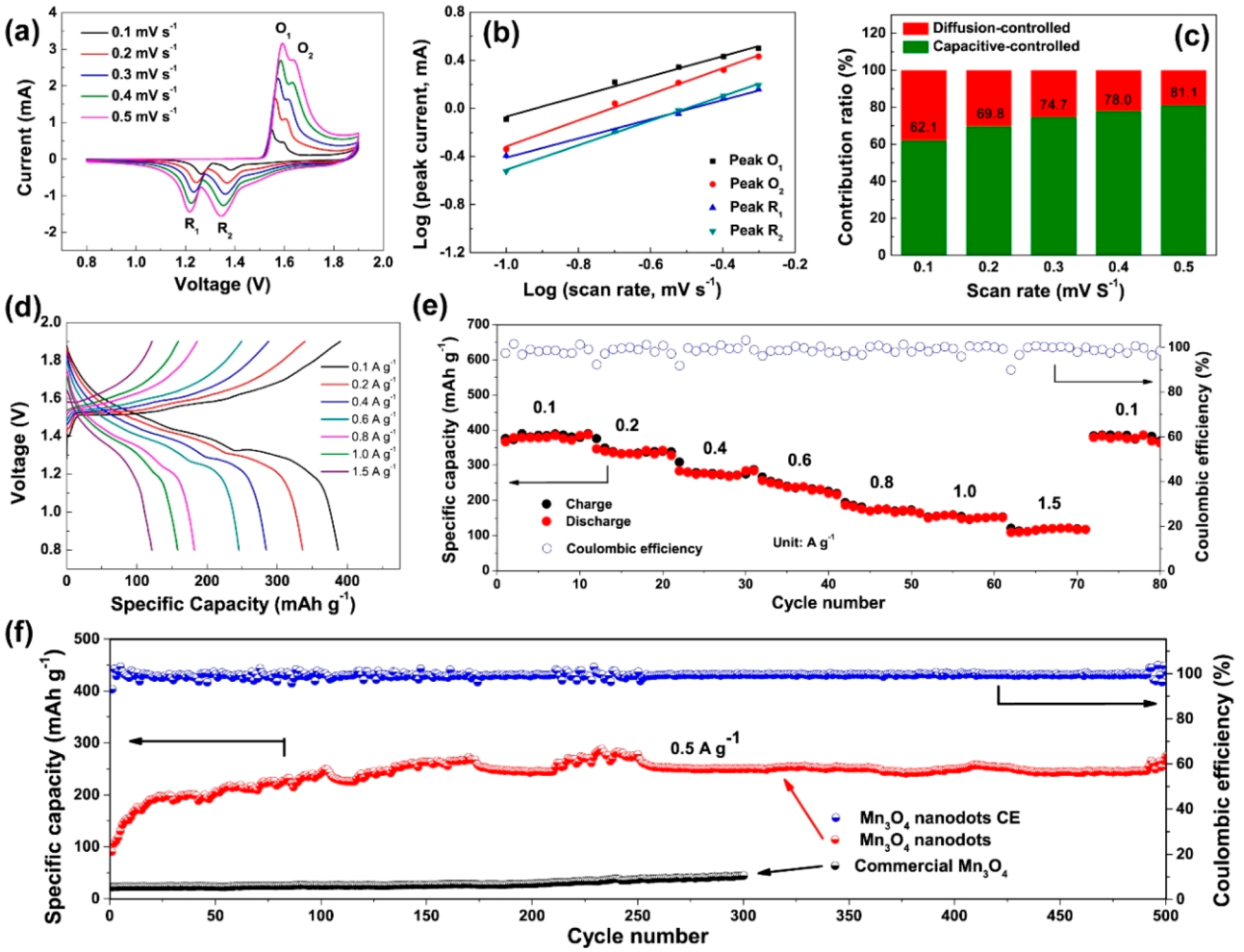

Figure 2. (a) Cyclic voltammograms of the Mn_3O_4 nanodot electrode at various scan rates from 0.1 to 0.5 mV s^{-1} from 0.9 to 1.9 V. (b) log *i* *vs* log *v* plots based on the CV profiles at four different oxidation/reduction states. (c) Contribution ratio of capacitive and diffusion-controlled capacities at different scan rates. (d) Charge/discharge profiles of the cell tested with different current densities from 0.1 to 1.5 A g^{-1}. (e) Rate performance of the as-assembled Zn-Mn_3O_4 coin cell. (f) Cycling performance of our Mn_3O_4 nanodots and commercial products.

It is known that the dimensions and exposed surface ratio of active materials significantly contribute to the electrochemical activity.[20−22] To the best of our knowledge, the size limit of the as-reported spinel cathode in ZIBs is 15−20 nm to date.[6,10] It is logical to determine if the size could be further diminished to a scale of several atoms? Enhanced Zn-ion storage performance would be found in nanodot samples of only several nanometers in size. In such a case, the number of activated surficial atoms drastically increases as the size deceases for ultrasmall nanostructures.[23] On the other hand, the Zn^{2+} and electron transfer pathway would be greatly shortened.[24,25] Consequently, the problem should be how to obtain a spinel structure on a scale of several nanometers toward their application in high-performance Zn-ion storage.

Inspired by this consideration, herein, we developed a general strategy toward ultrasmall spinel oxide nanodots (Mn_3O_4, $CoMn_2O_4$, $MnCo_2O_{4.5}$, Co_3O_4, and $ZnMn_2O_4$). The resulting Mn_3O_4 nanodots delivered the best Zn-ion storage ability including a high reversible capacity of 386.7 mA h g^{-1} at 0.1 A g^{-1}. The flexible ZIBs constructed from the Mn_3O_4 nanodot cathode deliver a high specific energy of 452 W h kg^{-1} at a power density of 141 W kg^{-1}. More importantly, an ultrahigh Zn^{2+} diffusion coefficient of 2.4×10^{-10} cm^2 s^{-1} has been detected during the discharge process. This value is more than 2 orders of magnitude higher than that of other spinel oxide nanostructures in previous reports and also the highest one in all of the as-reported values for various ZIB cathode materials to date. Our finding offers promising opportunities for the development of ZIB cathode materials with high energy density, long-term cycling stability, excellent flexibility, and wearability.

RESULTS AND DISCUSSION

Characterization of Ultrasmall Mn_3O_4 Nanodots. Ultrasmall Mn_3O_4 nanodots were synthesized by a two-step chemical process including refluxing and solvothermal treatment (Figure 1a). First, the precursor solution was achieved through a refluxing process in an oil bath using $NH_3{\cdot}H_2O$ as complexing agent. Subsequently, this precursor solution was treated by a solvothermal reaction in ethanol (EtOH) under 150 °C for 10 h. After the solvothermal treatment, some brown sediment was formed in the bottom of the autoclave. Interestingly, we found that the dispersity of the brown sediment can be drastically improved by changing the dispersant from EtOH to Mill-Q water. As shown in Figure 1f, a uniform colloidal suspension can be obtained with a clear Tyndall scattering by ultrasonically dispersing the product in Mill-Q water with a concentration of 0.5 mg mL^{-1}. The reason should be attributed to the much higher value of the zeta-potential in the Mill-Q water system

DOI: 10.1021/acsnano.9b04165
ACS Nano 2019, 13, 10376−10385

(+22.8 mV) than that in EtOH solvent (+2.48 mV). It is known that a large zeta-potential value of a nanoparticle means a high density of surface charge, generally resulting in a monodisperse suspension due to strong electrostatic repulsion among the building blocks in the solution. It is noteworthy that the great majority of oxide colloidal particles are negatively charged to date.[26,27] Surprisingly, our Mn_3O_4 nanodots produce a positively charged colloidal surface as the first example due to the presence of abundant oxygen vacancies (described below).

The X-ray diffraction (XRD) pattern with sharp diffraction peaks in Figure 1b can be well indexed to tetragonal Mn_3O_4 (JCPDS Card No. 80-0382) without any impurity. The Mn_3O_4 can be regarded as $[Mn^{2+}]_2[Mn^{4+}]O_4$ and crystallized in a spinel structure with space group $I4_1/amd$, where Mn^{4+} and Mn^{2+} separately take up the tetragonal (4a) sites and octahedral (8d) sites.[14,28] Transmission electron microscopy (TEM) characterization reveals that our sample consisted of a large number of nanodot-like objects with an average size of 6.0 nm (Figure 1g,h), which is much smaller than that of $ZnMn_2O_4$ nanoparticles reported previously (15−20 nm).[11] The corresponding high-resolution transmission electron microscopy (HRTEM) image exhibited a clear two-dimensional lattice fringe of 2.7 and 3.1 Å, which respectively corresponds to the *d*-spacing of tetragonal Mn_3O_4 (112) and (103) planes (Figure 1i). The selected area electron diffraction (SAED) pattern taken from several nanodots shows typical polycrystalline diffraction rings (Figure 1j). High-resolution X-ray photoelectron spectroscopy (XPS) characterization was performed to identify the oxidation state of Mn in our nanodots (Figure 1k). The high-resolution O 1s spectrum in Figure 1l can be resolved into two components centered at 529.2 and 531.1 eV, representing typical Mn−O−Mn and Mn−O−H bonds, respectively. The observation of a Mn−O−H bond suggests the presence of defective oxygen in the present nanodot samples.[29] The Mn 2p spectrum in Figure 1m can be well fitted into the Mn^{4+} 2p parts (642.7 and 654.5 eV) and Mn^{2+} 2p parts (640.9 and 652.7 eV), respectively. The Mn $2p_{3/2}$−$2p_{1/2}$ doublet with a splitting width of ∼11.8 eV is well consistent with that of Mn_3O_4 in previous reports.[12−14] In addition, XPS characterization indicates a molar ratio of ∼4:1 for Mn^{2+}/Mn^{4+} in the as-prepared sample, which is much higher than the value (2:1) in stoichiometric Mn_3O_4. This result also demonstrates the presence of abundant oxygen vacancies in the Mn_3O_4 nanocrystal, and the chemical formula of our product can be accurately depicted as $[Mn^{2+}_{2.4}][Mn^{4+}_{0.6}]O_{3.6}$. Inductively coupled plasma (ICP) analysis further confirms that the stoichiometric ratio of Mn:O is about 3:3.64, which is well consistent with the result from XPS characterization. The formation of a large number of oxygen vacancies should be ascribed to the solution alkalinity (pH ≈ 10.5) of the precursor solution. It has been revealed that the growing rate of nanoparticles becomes faster in an alkaline environment than that under neutral conditions, and such a rapid nucleation/growth process would lead to a large number of oxygen vacancies in the product.[30,31] We found that the Mn_3O_4 nanostructures synthesized in an EtOH/H_2O mixture (v/v = 1:1) (Figures S1, S2) exhibit a Mn:O stoichiometric ratio of 3:3.78 by ICP analysis. This ratio is slightly larger than that in pure EtOH solvent, suggesting a decreased oxygen vacancy concentration in the product by the introduction of a water phase during the solvothermal process. This successful preparation of Mn_3O_4 nanodots in a large scale should hold great promise for Zn-ion storage owing to their highly exposed surface and abundant oxygen vacancies.

Zn-Ion Storage Performance. Subsequently, a conventional CR-2032 coin cell was assembled with Mn_3O_4 nanodots (loading density was ∼2 mg cm^{-2}) as cathode, zinc foil as anode, glass fiber as separator, and a 2 M $ZnSO_4$/0.2 M $MnSO_4$ aqueous solution as electrolyte to evaluate the electrochemical performance on Zn-ion storage of our Mn_3O_4 nanodot cathode. As shown in Figure 2a, the cyclic voltammetry (CV) curves of this cell at various scan rates from 0.1 to 0.5 mV s^{-1} exhibit distinct oxidation peaks at 1.5 to 1.7 V, and the corresponding reduction peaks are located at 1.34 to 1.22 V, respectively. According to the previous study on a Zn-Mn_3O_4 battery, the Mn_3O_4 cathode first converts to layered birnessite-type MnO_2, and then Zn^{2+} and H^+ intercalation/deintercalation occurs in the layered birnessite phase.[12] The lower voltage peak at 1.22 V (R_1) corresponds to the insertion of Zn^{2+} into the interlayer of active manganese oxides, and the peak at 1.34 V (R_2) can be ascribed to H^+ intercalation.[12] Herein, *ex situ* XRD characterization (Figure S3) was conducted to investigate the phase evolution during the electrochemical process. After 100 cycles at 0.5 A g^{-1}, the peak intensity of Mn_3O_4 becomes weaker and some new diffraction peaks appear, which can be well indexed to Zn-birnessite, MnO(OH), and $3Zn(OH)_2{\cdot}ZnSO_4{\cdot}5H_2O$, respectively. The formation of MnO(OH) and $3Zn(OH)_2{\cdot}ZnSO_4{\cdot}5H_2O$ should provide direct evidence for the consumption of H^+ in the electrolyte and also H^+ intercalation in the cathode materials.[32]

To deeply understand the kinetics by separating the capacitive-controlled and diffusion-controlled capacity, the dependence of $\log(i_p)$ and $\log(v)$ at various scan rates is given in Figure 2b. It is known that the capacity contributed by the capacitive effect and battery-type effect (diffusion effect) can be distinguished according to the following equations:

$$i_p = av^b \tag{1}$$

$$I = C_1v + C_2v^{1/2} \tag{2}$$

where i_p is the peak current, I is the current at a fixed potential, v is the scan rate, and a, b, C_1, and C_2 are adjustable values. Whereas a b value of 0.5 indicates that the current is controlled by semi-infinite linear diffusion, and a value of 1.0 indicates that the current is surface-controlled. The b values determined by the slope of the $\log(i_d)$−$\log(v)$ plots are 0.83, 0.96, 0.79, and 0.94 for anodic peaks O_1 and O_2 and cathodic peaks R_1 and R_2 in Figure 2a, respectively. This result demonstrates that the capacitive process plays a major role in the whole capacity contribution to Zn-ion storage, which is favorable for fast kinetics.[33] The capacitive contribution is estimated to be 62.1%, 69.8%, 74.7%, 78.0%, and 81.1% at the scan rate of 0.1, 0.2, 0.3, 0.4, and 0.5 mV s^{-1}, respectively, indicating a little rise of the capacitive effect with the increase of the scan rate (Figures 2c, S4).

Notably, the as-assembled cell delivered reversible capacities of 386.7, 336.2, 284.4, 245.7, 182.3, 158.3, and 121.6 mA h g^{-1}, respectively, at current densities of 0.1, 0.2, 0.4, 0.6, 0.8, 1.0, and 1.5 A g^{-1}, which are significantly higher than the previous reported values on Mn_3O_4 cathodes.[12−15] When the current density was decreased back to 0.1 A g^{-1}, the capacity returned to 384.9 mA h g^{-1} (Figure 2d,e). Note that two discharge plateaus were observed in the charge/discharge profiles at a low current density in Figure 2d, respectively corresponding to the Zn^{2+} and H^+ intercalation as mentioned in Figure 2a.[12,32] The turning point at around 1.3 V could be ascribed to the sudden slowing down of the ion diffusion coefficient (described below).[34,35] The

DOI: 10.1021/acsnano.9b04165
ACS Nano 2019, 13, 10376−10385

long-term cycling stability was further investigated with commercial Mn_3O_4 powder as the counterpart sample at a current density of 0.5 A g^{-1} (Figure 2f). One can see that the commercial product shows only a rather low capacity of ~40 mA h g^{-1} within 300 cycles. In contrast, our nanodots exhibit greatly enhanced capacity and long-life stability without capacity fading after 500 charge/discharge cycles. The initial discharge capacity of our Mn_3O_4 nanodots is 90.7 mA h g^{-1}, and then it gradually increases and remains at ~245 mA h g^{-1}, which should be attributed to the progressive conversion reactions and improved electrochemical activity of the newly formed birnessite phase during the discharge process.[12] Note that the Mn^{2+} ion dissolution phenomenon has been observed in our nanodot sample, confirmed by XPS characterization after 100 cycles of glass fiber separator in a Zn foil//Mn_3O_4 nanodot battery using unitary $ZnSO_4$ salt as the electrolyte (Figure S5). Moreover, the electrolyte additive of $MnSO_4$ reduces the Mn^{2+} ion dissolution into the electrolyte, resulting in the higher capacity and better long-term cycling performance (Figure S6).[14,15]

Figure 3a compares the rate performance between the present Mn_3O_4 nanodots with other Mn_3O_4 nanostructures recently

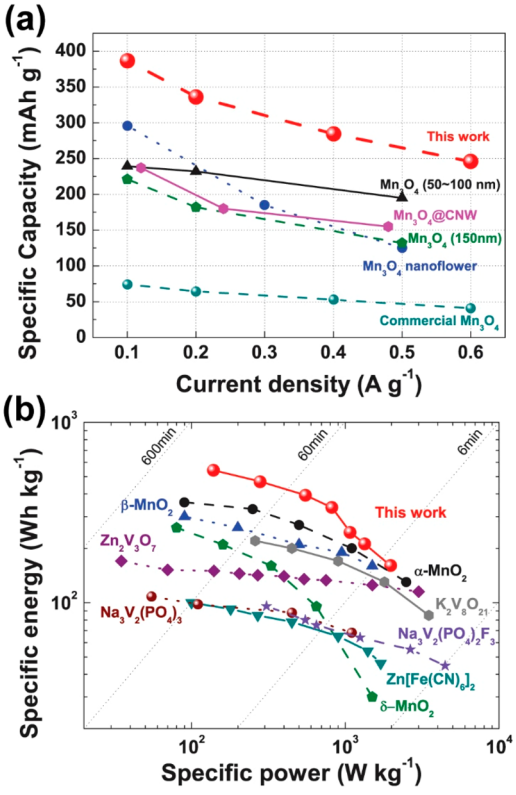

Figure 3. (a) Comparison of the rate performance of our Mn_3O_4 nanodots, other recently reported Mn_3O_4 nanostructures, and commercial products. (b) Comparison of the Ragone plot of Mn_3O_4 nanodots and other reported cathode materials for ZIBs.

reported[12−15] and commercial products (Figures S7−S9). It is clear that the high specific capacity of our sample is much higher than that of the other samples over the current density from 0.1 to 0.6 A g^{-1} (Table 1, Table S1). The Ragone plots (Figure 3b) further display the high energy and high power density of the Mn_3O_4 nanodot-based ZIBs. Clearly, our ZIBs possess a high specific energy of 543 W h kg^{-1} at 0.1 A g^{-1} and maintain 160 W h kg^{-1} at a high power rate of 1973 W kg^{-1}, which surpasses that

Table 1. Comparison for D_{Zn} at the Discharge Plateau and Specific Capacity of Various Cathode Materials in ZIBs

cathode	D_{Zn} at discharge plateau (cm^2 s^{-1})	specific capacity	ref
Mn_3O_4 nanodots	2.4×10^{-10}	386.7 mA h g^{-1} at 0.1 A g^{-1}	this work.
Mn_3O_4 nanoflowers	10^{-12}	296 mA h g^{-1} at 0.1 A g^{-1}	11
$ZnMn_2O_4$	4×10^{-12}	~150 mA h g^{-1} at 0.05 A g^{-1}	13
$K_2V_8O_{21}$	1.99×10^{-11} to 2.33×10^{-10}	226 mA h g^{-1} at 0.5 A g^{-1}	40
$K_{0.25}V_2O_5$	1.015×10^{-11} to 1.14×10^{-10}	~175 mA h g^{-1} at 0.5 A g^{-1}	40
$K_2V_6O_{16}\cdot 1.57H_2O$	6.75×10^{-12} to 2.10×10^{-11}	~80 mA h g^{-1} at 0.5 A g^{-1}	40
KV_3O_8	4.96×10^{-12} to 3.75×10^{-11}	~50 mA h g^{-1} at 0.5 A g^{-1}	40
$H_2V_3O_8$	5×10^{-11} to 1.5×10^{-10}	423.8 mA h g^{-1} at 0.1 A g^{-1}	45
VO_2	10^{-11}	357 mA h g^{-1} at 0.1 A g^{-1}	46

of most recent ZIBs based on α, β, δ-MnO_2,[36−38] $Zn_2V_2O_7$,[39] $K_2V_8O_{21}$,[40] $Na_3V_2(PO_4)_3$,[41] $Na_3V_2(PO_4)_2F_3$,[42] and $Zn[Fe(CN)_6]$.[43]

Recent rapid development of modern electronics has simulated rising requirements for energy storage devices with excellent flexibility and wearability. We further fabricated flexible Zn-ion batteries to confirm the flexible application of our nanodots. As illustrated in Figure 4a, the soft-packed batteries were assembled by pressing a stainless steel (SS) foil cathode coated with Mn_3O_4 nanodots (loading density was ~2 mg cm^{-2}), a zinc foil, and a separator into a sandwich structure and then sealing by Al plastic films. Figure 4b presents its charge/discharge profiles within the voltage window of 0.8 to 1.9 V for 10 cycles bent at 45° at 0.5 A g^{-1}. The flexible ZIBs constructed from our Mn_3O_4 nanodot cathode deliver a high specific energy of 452 W h kg^{-1} at a power density of 141 W kg^{-1}. A single battery was able to light up a red light-emitting diode (LED) indicator (Figure 4c and Supplementary Video 1). The wristband LED indicator demonstrated the outstanding flexibility and stability of our Zn-Mn_3O_4 nanodot battery, which would show very promising potential in next-generation portable and wearable devices (Figure 4d,e).

Ultrafast Diffusion Kinetics. To deeply understand the origin of the superior performance in capacity and long-term stability of the Zn-Mn_3O_4 nanodot battery, electrochemical impedance spectra (EIS) measurement was performed and is shown in Figure 5a. The typical Nyquist plots consist of a semicircle and a sloping straight line at the low-frequency region. It is clear that our Mn_3O_4 nanodots possess a rather low charge transfer resistance and smaller Warburg impedance than commercial products, demonstrating its faster charge transfer and ionic diffusion ability. Galvanostatic intermittent titration technique (GITT) measurement has been further utilized to reveal the diffusion coefficient (D) in our Mn_3O_4 nanodots (Figure 5b). In general, D can be calculated based on the following equation:[44]

$$D = \frac{4}{\pi\tau}\left(\frac{n_m V_m}{S}\right)^2\left(\frac{\Delta E_s}{\Delta E_t}\right)^2 \quad (3)$$

where τ is the relaxation time of the current pulse, n_m and V_m are the mole number and mole volume of the active material, S is the

DOI: 10.1021/acsnano.9b04165
ACS Nano 2019, 13, 10376−10385

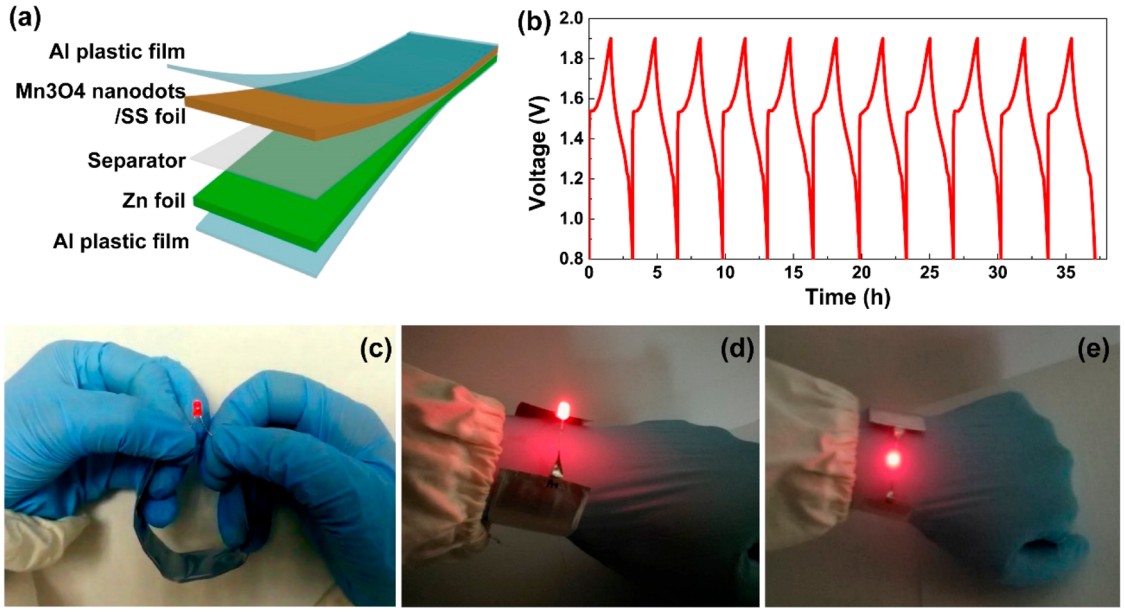

Figure 4. (a) Schematic structure of the flexible Zn-Mn_3O_4 nanodot battery constructed on flexible current collectors. (b) Charge/discharge profiles (voltage *versus* time) of the soft-packed battery bent at 45° at 0.5 A g^{-1}. (c) Photograph of a red light-emitting diode indicator lighted by a single battery. (d) Side view and (e) top view of a wearable light-emitting diode indicator wristband lighted by a single battery.

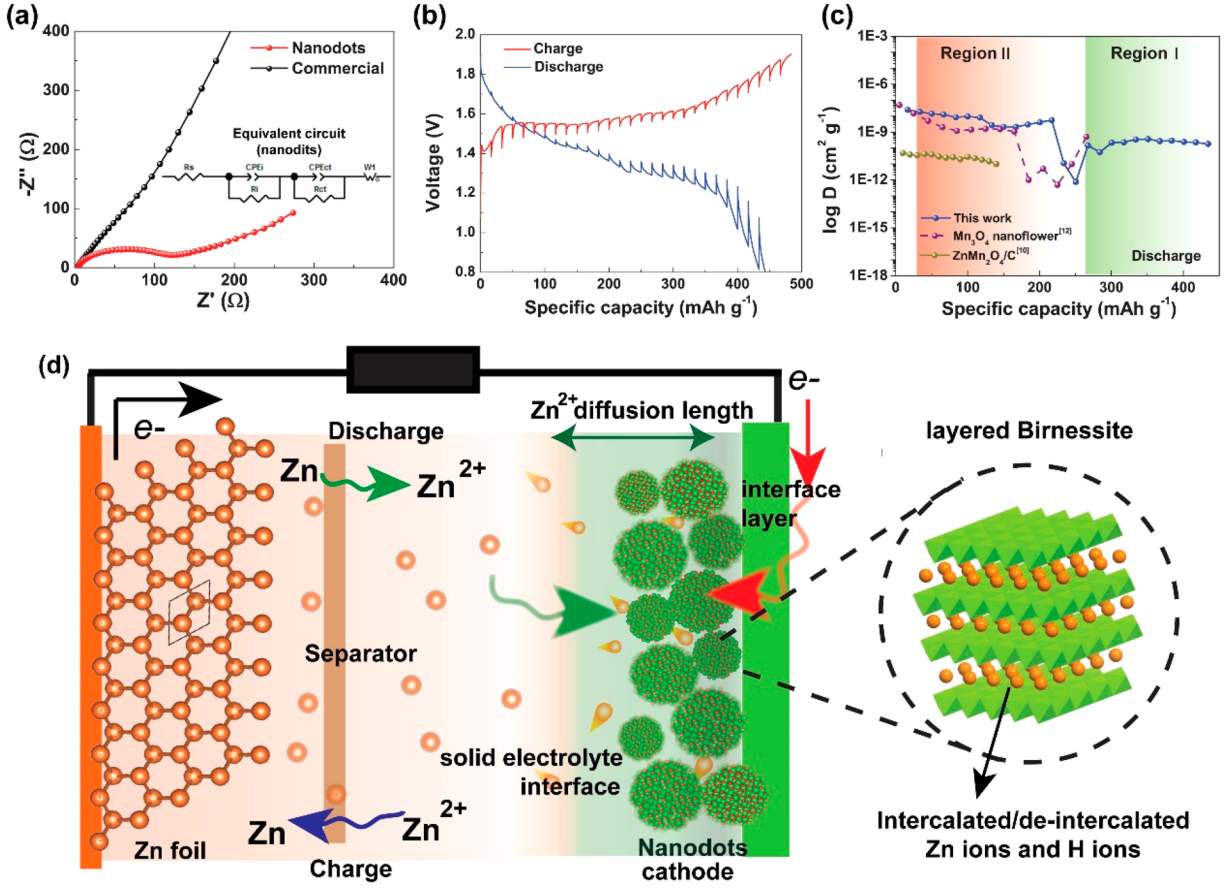

Figure 5. (a) Electrochemical impedance spectra of the Zn-Mn_3O_4 nanodot battery and the corresponding fitting equivalent circuit (inset). R_s, R_i, R_{ct}, and W_1 represent solution resistance, interface resistance, charge transfer resistance, and Warburg impedance, respectively. (b) GITT profiles of the Zn-Mn_3O_4 nanodot battery. (c) Zn-ion diffusion coefficient in the discharge process calculated by GITT profiles and those in previous reports.[11,13] (d) Schematic representation of the Zn-ion transport in the Zn-Mn_3O_4 nanodot battery.

contacting area between the electrode and the electrolyte, ΔE_s is the voltage change induced by the current pulse, and ΔE_t is the voltage change caused by the galvanostatic charge/discharge. The contacting area (S) was calculated by the following formula:

DOI: 10.1021/acsnano.9b04165
ACS Nano 2019, 13, 10376−10385

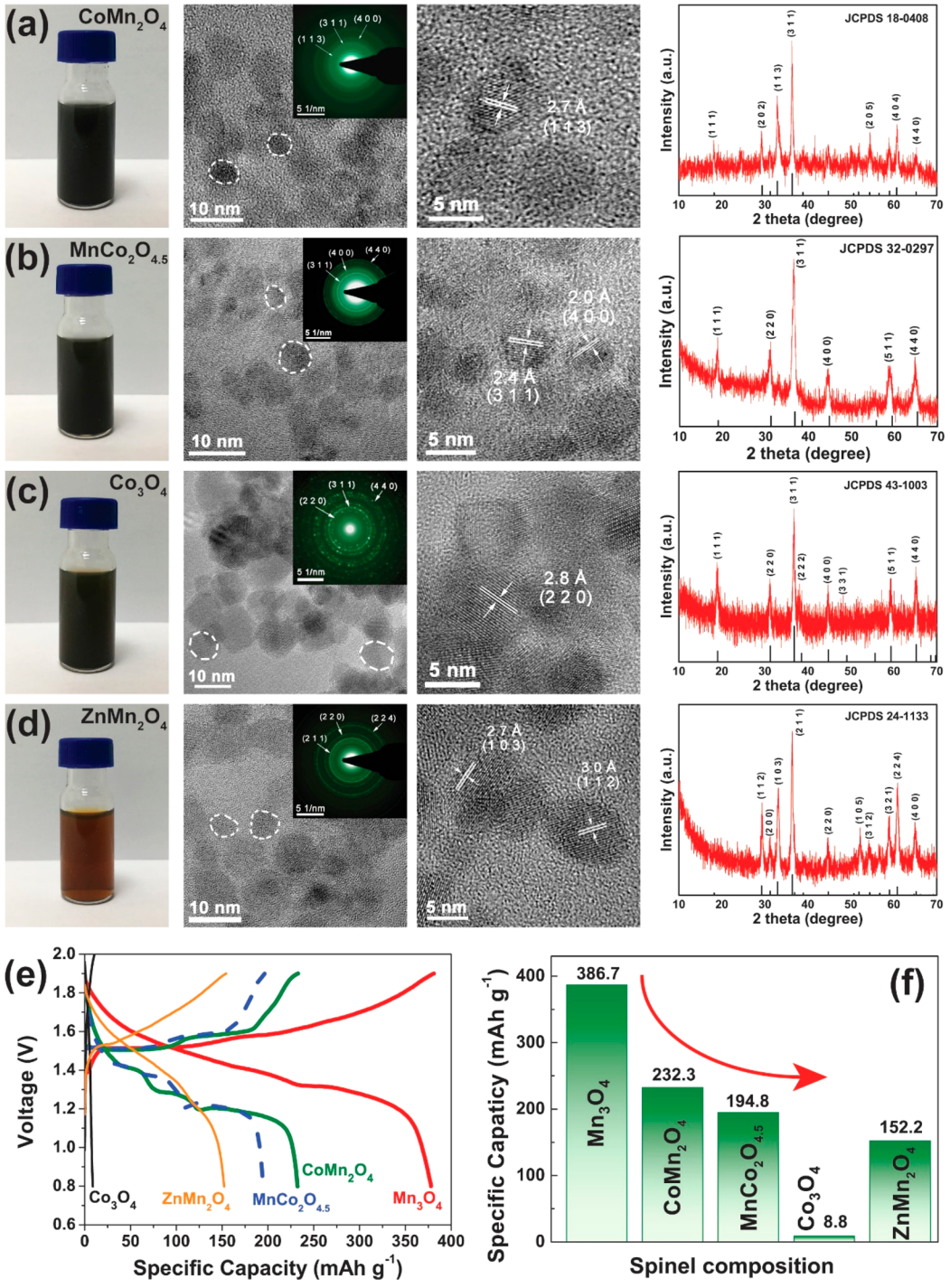

Figure 6. Optical images, TEM images, SAED patterns (inset), HRTEM images, and powder XRD patterns of (a) $CoMn_2O_4$, (b) $MnCo_2O_{4.5}$, (c) Co_3O_4, and (d) $ZnMn_2O_4$ nanodots. (e) Typical galvanostatic charge/discharge curves at 0.1 A g^{-1} of as-prepared spinel oxide nanodots. (f) Comparison of specific capacity of $Mn_xCo_{3-x}O_y$ (x = 0, 1, 2, 3; y = 4, 4.5) series and $ZnMn_2O_4$ nanodots.

$S = m\Delta S$, where m is the weight of active materials and ΔS is the specific surface area obtained by the Brunauer–Emmett–Teller (BET) method (Figure S10). Surprisingly, the average D_{Zn} value at the discharge and charge plateau calculated by GITT profiles are as high as 2.4×10^{-10} and 5.1×10^{-10} cm^2 s^{-1}, respectively (Figures 5c, S11). This value is more than 2 orders of magnitude higher than that of other spinel oxide nanostructures in previous reports.[11,13] More importantly, to the best of our knowledge, it is the highest one in all of the as-reported values for various ZIB cathode materials to date (Table 1).[40,45,46] It is rational that highly activated surficial atoms in the nanodots should drastically facilitate the Zn ion diffusion and transport. As determined by the N_2 adsorption measurement, the BET specific surface area of our nanodot sample is 59.1 cm^2 g^{-1}. Note that the nanodots are very easily aggregated during the N_2 adsorption measurement, and the real surface area should be much higher than this value. In contrast, the commercial Mn_3O_4 sample with an average particle size of 3.3 μm just exhibits a much lower specific surface area of 0.59 cm^2 g^{-1} (Figures S8, S12). Second, the introduction of numerous oxygen vacancies

DOI: 10.1021/acsnano.9b04165
ACS Nano 2019, 13, 10376–10385

into nanostructures have been proved to be an effective way to enhance the diffusion kinetics and electrochemical performance of metal oxides.[47] The presence of oxygen vacancies in the as-prepared nanodots can act as active sites for electrochemical reactions and produce higher electrical conductivity.[48,49]

Such a high Zn^{2+}diffusion coefficient (D) in our Mn_3O_4 nanodots should be the origin of the superior performance in energy density and power density (rate performance). Figure 4d schematically interprets the working principle and ion transport details in our nanodot-based batteries. Previous studies have confirmed the phase evolution of the Mn_3O_4 cathode during the charge/discharge cycling: Mn_3O_4 spinel first converts to layered birnessite, and then Zn ion was intercalated/deintercalated in the layered birnessite phase *via* a reversible intercalation pathway.[12] During the dischage process, Zn^{2+} has to go through the solid electrolyte interphase (SEI) layer and then enter the active, layered birnessite. Meanwhile, the electrons also pass through a certain diffusion length in the interface layer for this intercalated/deintercalated electrochemical reaction. For the charging process, both Zn ions and electrons move along opposite directions. As the effective diffusion length was shortened, a greater portion of active materials would participate in the electrochemical reaction. According to the discussion of Zhu *et al.*, the characteristic diffusion time (τ^*), which denotes the minimum time required for the ions/electrons to move through the batteries, can be defined as[50]

$$\tau^* = L^2/\alpha D \quad (4)$$

where L is the particle radius or half-thickness, α is a geometric factor, and D is the effective diffusion coefficient of charge pieces (Zn^{2+}/e^-) inside the electrode. However, in the case of our spherical nanodot samples, L can be regarded as small as 3 nm, α equals 0.15 under constant current,[50] and the average D_{Zn} value is as high as 2.4×10^{-10} cm^2 s^{-1}. Accordingly, τ^* is calculated to be 2.5×10^{-5} s for our nanodots. It is known that if the charge/discharge time is shorter than τ^*, the interaction reaction cannot be completed, leading to a loss of capacity. Therefore, such a lower value of τ^* in our nanodot sample corresponds to an ultrafast Zn ion diffusion kinetics and gives rise to a superior rate performance or power density, as shown in Figure 3.

Nanodots for the Spinel Oxide Family. We finally confirm this growth strategy can be easily extended to other spinel samples including $CoMn_2O_4$, $MnCo_2O_{4.5}$, Co_3O_4, and $ZnMn_2O_4$, the crystallographic information of which are listed in Table S2. A highly stable colloidal suspension has also been respectively achieved in these components (Figure 6a–d). Typical TEM and HRTEM observation indicates the morphology of monodispersed nanocrystals with a size ranging from 4 to 8 nm for these samples. Their phase purity and chemical composition were verified by the corresponding XRD patterns and energy dispersive spectroscopy (EDS) in Figures S13–S15. In order to reveal the composition-tuned Zn-ion storage capacity in all of these spinel nanodots, we compare the galvanostatic charge/discharge curves of these spinel nanodot-based ZIBs (Figure 6e). We found that Mn_3O_4 shows the highest specific capacity among the spinel family $Mn_xCo_{3-x}O_y$ (x = 0, 1, 2, 3; y = 4, 4.5) (Figures 6f, S16–S19). The Zn-ion storage capacity gradually decreases with reducing manganese concentration in this $Mn_xCo_{3-x}O_4$ series. It is known that metal oxides with a cobalt component work in an alkaline electrolyte ZIB system in previous reports.[48,51,52] Accordingly, the as-observed decrease tendency on capacity should be attributed to the poor activity of cobalt(II) in mild aqueous electrolyte conditions.

CONCLUSION

In summary, we have developed a general synthesis strategy to prepare ultrasmall spinel oxide nanodots (Mn_3O_4, $CoMn_2O_4$, $MnCo_2O_{4.5}$, Co_3O_4, and $ZnMn_2O_4$) in a high yield. Among them, Mn_3O_4 nanodots delivered the best Zn-ion storage ability including a high reversible capacity of 386.7 mA h g^{-1} at 0.1 A g^{-1}, excellent rate performance, and a long-term stability of 500 cycles at 0.5 A g^{-1}. The flexible ZIBs constructed from our Mn_3O_4 nanodot cathode deliver a high specific energy of 452 W h kg^{-1} at a power density of 141 W kg^{-1}. More importantly, an ultrahigh Zn^{2+} diffusion coefficient of 2.4×10^{-10} cm^2 s^{-1} has been detected during the discharge process. This value is more than 2 orders of magnitude higher than that of other spinel oxide nanostructures in previous reports and also the highest one of all of the as-reported ZIB cathode materials to date. Our finding offers promising opportunities for the development of rechargeable ZIB cathode materials with high energy density, long-term cycling stability, excellent flexibility, and wearability. They also hold promise for applications in other metal ion storage (Li^+, K^+, Na^+, Ca^{2+}, *etc.*) for next-generation electrochemical energy storage devices. Furthermore, the positively charged nature of our spinel nanodots would provide abundant opportunities for electrostatic self-assembly with other negatively charged colloidal particles (graphene, MXenes, MoS_2, *etc.*) for enhanced energy storage applications by synergistic effects.

EXPERIMENTAL SECTION

Preparation of Spinel Nanodots. In a typical synthesis of Mn_3O_4 nanodots, 4.5 mmol of $Mn(OAc)_2{\cdot}4H_2O$ was dissolved in 225 mL of ethanol, and then 1.5 mL of 25% ammonia solution was added. After stirring at 80 °C for 2 h, the solution was transferred into a 100 mL Teflon-lined autoclave and maintained at 150 °C for 10 h. The product was collected by micromembrane filtration, washed with ethanol three times, and dried at 60 °C for 12 h. For the synthesis of $Mn_xCo_{3-x}O_y$ (x = 0, 1, 2, 3; y = 4, 4.5), 1.5x mmol of $Mn(OAc)_2{\cdot}4H_2O$ and (4.5−1.5x) mmol of $Co(OAc)_2{\cdot}4H_2O$ were dissolved to prepare the precursor, respectively, while 1.5 mmol of $Zn(OAc)_2{\cdot}2H_2O$ and 3 mmol of $Mn(OAc)_2{\cdot}4H_2O$ were added for $ZnMn_2O_4$ sample.

Material Characterization. The crystalline structure of oxide nanodots was characterized by powder XRD (Bruker D8 Advance with Cu Kα radiation). The morphology and elemental composition were determined by scanning electron microscopy (SEM, Phenom Pro X) and HRTEM (FEI TECNAI G^2 S-TWIN) with EDS. The valence variation was determined by XPS (PHI 5000C and PHI 5300). The concentration of Mn of the Mn_3O_4 nanodot sample was obtained by ICP (PerkinElemer Optima8000). The specific surface area was obtained using BET (Quadrasorb evo) method.

Battery Assembly. The 2032 coin cells were assembled with zinc foil as anode, glass fiber as separator, and 2 M $ZnSO_4$/0.2 M $MnSO_4$ aqueous solution as electrolyte. Typically, the cathode was prepared with oxide nanodots as active material, acetylene black as conductive agent, and polyvinylidene fluoride as binder (weight ratio = 7:2:1). The mixture was blended in *N*-methyl-2-pyrrolidone and cast onto 304L SS foil with a thickness of 150 μm. The electrode was vacuum-dried at 80 °C for 12 h, and the typical loading density of nanodots was ∼2 mg cm^{-2}. The soft-packed batteries were obtained by pressing a piece of such cathode, a zinc foil, and a nonwoven fabric separator into a sandwich structure.

Electrochemical Measurement. Galvanostatic charge−discharge tests with a voltage window from 0.8 to 1.9 V were carried out on a battery test system (LAND CT2001A). GITT measurements were performed at 0.1 A g^{-1} for 10 min followed by a 10 min rest. CV tests

DOI: 10.1021/acsnano.9b04165
ACS Nano 2019, 13, 10376−10385

from 0.1 to 0.5 mV s^{-1} and EIS from 10^6 to 0.01 Hz were conducted on a electrochemical workstation (CHI 600E). The electrochemical performance was calculated based on the loading mass of the active materials (nanodots).

ASSOCIATED CONTENT

Supporting Information

The Supporting Information is available free of charge on the ACS Publications website at DOI: 10.1021/acsnano.9b04165.

XRD, TEM, EDS, XPS, SEM, BET method results, and electrochemical performance (Figure S1−S19); comparison of rate performance of cathode materials in ZIBs (Table S1), crystallographic information of the as-prepared spinel oxide nanodots (Table S2), and references (PDF)

Movie M1 (AVI)

AUTHOR INFORMATION

Corresponding Author

*E-mail: linfenghu@fudan.edu.cn.

ORCID

Linfeng Hu: 0000-0002-0640-508X

Notes

The authors declare no competing financial interest.

ACKNOWLEDGMENTS

This work was financially supported by the National Natural Science Foundation of China (Nos. 51872051, 51701042), the Science and Technology Committee of Shanghai Municipality (18520723100), and the Researching Program of State Grid Corporation of China (GYW17201800011).

REFERENCES

(1) Arico, A. S.; Bruce, P.; Scrosati, B.; Tarascon, J.-M.; Schalkwijk, W. V. Nanostructured Materials for Advanced Energy Conversion and Storage Devices. *Nat. Mater.* **2005**, *4*, 366−377.

(2) Lin, D.; Liu, Y.; Cui, Y. Reviving the Lithium Metal Anode for High-Energy Batteries. *Nat. Nanotechnol.* **2017**, *12*, 194−206.

(3) Zhao, Y.; Li, X.; Yan, B.; Xiong, D.; Li, D.; Lawes, S.; Sun, X. Recent Developments and Understanding of Novel Mixed Transition-Metal Oxides as Anodes in Lithium Ion Batteries. *Adv. Energy Mater.* **2016**, *6*, 1502175.

(4) Li, H.; Han, C.; Huang, Y.; Huang, Y.; Zhu, M.; Pei, Z.; Xue, Q.; Wang, Z.; Liu, Z.; Tang, Z.; Wang, Y.; Kang, F.; Li, B.; Zhi, C. Y. An Extremely Safe and Wearable Solid-State Zinc Ion Battery Based on a Hierarchical Structured Polymer Electrolyte. *Energy Environ. Sci.* **2018**, *11*, 941−951.

(5) Ma, L.; Chen, S.; Li, H.; Ruan, Z.; Tang, Z.; Liu, Z.; Wang, Z.; Huang, Y.; Pei, Z.; Zapien, J. A.; Zhi, C. Y. Initiating a Mild Aqueous Electrolyte Co_3O_4/Zn Battery with 2.2 V-High Voltage and 5000-Cycle Lifespan by a Co(III) Rich-Electrode. *Energy Environ. Sci.* **2018**, *11*, 2521−2530.

(6) Song, M.; Tan, H.; Chao, D.; Fan, H. J. Recent Advances in Zn-Ion Batteries. *Adv. Funct. Mater.* **2018**, *28*, 1802564.

(7) Hu, P.; Zhu, T.; Wang, X.; Wei, X.; Yan, M.; Li, J.; Luo, W.; Yang, W.; Zhang, W.; Zhou, L.; Zhou, Z.; Mai, L. Q. Highly Durable $Na_2V_6O_{16}{\cdot}1.63H_2O$ Nanowire Cathode for Aqueous Zinc-Ion Battery. *Nano Lett.* **2018**, *18*, 1758−1763.

(8) He, P.; Zhang, G.; Liao, X.; Yan, M.; Xu, X.; An, Q.; Liu, J.; Mai, L. Q. Sodium Ion Stabilized Vanadium Oxide Nanowire Cathode for High-Performance Zinc-Ion Batteries. *Adv. Energy Mater.* **2018**, *8*, 1702463.

(9) Li, Y.; Fu, J.; Zhong, C.; Wu, T.; Chen, Z.; Hu, W.; Amine, K.; Lu, J. Recent Advances in Flexible Zinc-Based Rechargeable Batteries. *Adv. Energy Mater.* **2019**, *9*, 1802605.

(10) Fang, G.; Zhou, J.; Pan, A.; Liang, S. Recent Advances in Aqueous Zinc-Ion Batteries. *ACS Energy Lett.* **2018**, *3*, 2480−2501.

(11) Zhang, N.; Cheng, F.; Liu, Y.; Zhao, Q.; Lei, K.; Chen, C.; Liu, X.; Chen, J. Cation-Deficient Spinel $ZnMn_2O_4$ Cathode in $Zn(CF_3SO_3)_2$ Electrolyte for Rechargeable Aqueous Zn-Ion Battery. *J. Am. Chem. Soc.* **2016**, *138*, 12894−12901.

(12) Hao, J.; Mou, J.; Zhang, J.; Dong, L.; Liu, W.; Xu, C.; Kang, F. Electrochemically Induced Spinel-Layered Phase Transition of Mn_3O_4 in High Performance Neutral Aqueous Rechargeable Zinc Battery. *Electrochim. Acta* **2018**, *259*, 170−178.

(13) Zhu, C.; Fang, G.; Zhou, J.; Guo, J.; Wang, Z.; Wang, C.; Li, J.; Tang, Y.; Liang, S. Binder-Free Stainless Steel@Mn_3O_4 Nanoflower Composite: a High-Activity Aqueous Zinc-Ion Battery Cathode with High-Capacity and Long-Cycle-Life. *J. Mater. Chem. A* **2018**, *6*, 9677−9683.

(14) Ma, L.; Li, L.; Liu, Y.; Zhu, J.; Meng, T.; Zhang, H.; Jiang, J.; Li, C. M. Building Better Rechargeable Zn-Mn Batteries with a Highly Active Mn_3O_4/Carbon Nanowire Cathode and Neutral Na_2SO_4/$MnSO_4$ Electrolyte. *Chem. Commun.* **2018**, *54*, 10835−10838.

(15) Wang, L.; Cao, X.; Xu, L.; Chen, J.; Zheng, J. Transformed Akhtenskite MnO_2 from Mn_3O_4 as Cathode for a Rechargeable Aqueous Zinc Ion Battery. *ACS Sustainable Chem. Eng.* **2018**, *6*, 16055−16063.

(16) Soundharrajan, V.; Sambandam, B.; Kim, S.; Mathew, V.; Jo, J.; Kim, S.; Lee, J.; Islam, S.; Kim, K.; Sun, Y.-K.; Kim, J. Aqueous Magnesium Zinc Hybrid Battery: an Advanced High-Voltage and High-Energy $MgMn_2O_4$ Cathode. *ACS Energy Lett.* **2018**, *3*, 1998−2004.

(17) Wu, X.; Xiang, Y.; Peng, Q.; Wu, X.; Li, Y.; Tang, F.; Song, R.; Liu, Z.; He, Z.; Wu, X. Green-Low-Cost Rechargeable Aqueous Zinc-Ion Battery Using Hollow Porous Spinel $ZnMn_2O_4$ as the Cathode Material. *J. Mater. Chem. A* **2017**, *5*, 17990−17997.

(18) Pan, C.; Nuzzo, R. G.; Gewirth, A. A. $ZnAl_xCo_{2-x}O_4$ Spinels as Cathode Materials for Non-Aqueous Zn Batteries with an Open Circuit Voltage of ≤ 2 V. *Chem. Mater.* **2017**, *29*, 9351−9359.

(19) Pan, C.; Zhang, R.; Nuzzo, R. G.; Gewirth, A. A. $ZnNi_xMn_xCo_{2-2x}O_4$ Spinel as a High-Voltage and High-Capacity Cathode Material for Nonaqueous Zn-Ion Batteries. *Adv. Energy Mater.* **2018**, *8*, 1800589.

(20) Tiwari, J. N.; Tiwari, R. N.; Kim, K. S. Zero-Dimensional, One-Dimensional, Two-Dimensional and Three-Dimensional Nanostructured Materials for Advanced Electrochemical Energy Devices. *Prog. Mater. Sci.* **2012**, *57*, 724−803.

(21) Wei, Q.; Xiong, F.; Tan, S.; Huang, L.; Lan, E. H.; Dunn, B.; Mai, L. Q. Porous One-Dimensional Nanomaterials: Design, Fabrication and Applications in Electrochemical Energy Storage. *Adv. Mater.* **2017**, *29*, 16022300.

(22) Chen, K. X.; Li, L. Ordered Structures with Functional Units as a Paradigm of Material Design. *Adv. Mater.* **2019**, 1901115.

(23) Wu, P.; Xu, Y.; Zhan, J.; Li, Y.; Xue, H.; Pang, H. The Research Development of Quantum Dots in Electrochemical Energy Storage. *Small* **2018**, *14*, 1801479.

(24) Tu, Z.; Yang, G.; Song, H.; Wang, C. Amorphous ZnO Quantum Dot/Mesoporous Carbon Bubble Composites for a High-Performance Lithium-Ion Battery Anode. *ACS Appl. Mater. Interfaces* **2017**, *9*, 439−446.

(25) Javed, M.; Saqib, A. N. S.; Ata-ur-Rehman; Ali, B.; Faizan, M.; Anang, D. A.; Iqbal, Z.; Abbas, S. M. Carbon Quantum Dots from Glucose Oxidation as a Highly Competent Anode Material for Lithium and Sodium-Ion Batteries. *Electrochim. Acta* **2019**, *297*, 250−257.

(26) Cai, X.; Ozawa, T. C.; Funatsu, A.; Ma, R.; Ebina, Y.; Sasaki, T. Tuning the Surface Charge of 2D Oxide Nanosheets and the Bulk-Scale Production of Superlatticelike Composites. *J. Am. Chem. Soc.* **2015**, *137*, 2844−2847.

(27) Ma, R.; Sasaki, T. Two-Dimensional Oxide and Hydroxide Nanosheets: Controllable High-Quality Exfoliation, Molecular Assembly, and Exploration of Functionality. *Acc. Chem. Res.* **2015**, *48*, 136−143.

(28) Raj, A. M. E.; Victoria, S. G.; Jothy, V. B.; Ravidhas, C.; Wollschlager, J.; Suendorf, M.; Neumann, M.; Jayachandran, M.;

Sanjeeviraja, C. XRD and XPS Characterization of Mixed Valence Mn_3O_4 Hausmannite Thin Films Prepared by Chemical Spray Pyrolysis Technique. *Appl. Surf. Sci.* **2010**, *256*, 2920−2926.
(29) Zhang, H.; Wang, J.; Liu, Q.; He, W.; Lai, Z.; Zhang, X.; Yu, M.; Tong, Y.; Lu, X. Extracting oxygen anions from $ZnMn_2O_4$: Robust Cathode for Flexible All-solid-state Zn-ion Batteries. *Energy Storage Mater.* **2018**, DOI: 10.1016/j.ensm.2018.12.019.
(30) Lee, Y. B.; Kim, S. K.; Lim, Y. R.; Jeon, I. S.; Song, W.; Myung, S.; Lee, S. S.; Lim, J.; An, K.-S. Dimensional-Hybrid Structures of 2D Materials with ZnO Nanostructures *via* pH-Mediated Hydrothermal Growth for Flexible UV Photodetectors. *ACS Appl. Mater. Interfaces* **2017**, *9*, 15031−15037.
(31) Ekthammathat, N.; Thongtem, T.; Phuruangrat, A.; Thongtem, S. Growth of Hexagonal Prism ZnO Nanorods on Zn Substrates by Hydrothermal Method and Their Photoluminescence. *Ceram. Int.* **2013**, *39*, S501.
(32) Huang, J.; Wang, Z.; Hou, M.; Dong, X.; Liu, Y.; Wang, Y.; Xia, Y. Polyaniline-Intercalated Manganese Dioxide Nanolayers as a High-Performance Cathode Material for an Aqueous Zinc-Ion Battery. *Nat. Commun.* **2018**, *9*, 2906.
(33) Shen, L.; Lv, H.; Chen, S.; Kopold, P.; Aken, P. A.; Wu, X.; Maier, J.; Yu, Y. Peapod-Like Li_3VO_4/N-Doped Carbon Nanowires with Pseudocapacitive Properties as Advanced Materials for High-Energy Lithium-Ion Capacitors. *Adv. Mater.* **2017**, *29*, 1700142.
(34) Liu, Y.; Zhou, X.; Liu, R.; Li, X.; Bai, Y.; Xiao, H.; Wang, Y.; Yuan, G. Tailoring Three-Dimensional Composite Architecture for Advanced Zinc-Ion Batteries. *ACS Appl. Mater. Interfaces* **2019**, *11*, 19191−19199.
(35) Wu, B.; Zhang, G.; Yan, M.; Xiong, T.; He, P.; He, L.; Xu, X.; Mai, L. Q. Graphene Scroll-Coated α-MnO_2 Nanowires as High-Performance Cathode Materials for Aqueous Zn-Ion Battery. *Small* **2018**, *14*, 1703850.
(36) Pan, H.; Shao, Y.; Yan, P.; Cheng, Y.; Han, K. S.; Nie, Z.; Wang, C.; Yang, J.; Li, X.; Bhattacharya, P.; Mueller, K. T.; Liu, J. Reversible Aqueous Zinc/Manganese Oxide Energy Storage from Conversion Reactions. *Nat. Energy* **2016**, *1*, 16039.
(37) Zhang, N.; Cheng, F.; Liu, J.; Wang, L.; Long, X.; Liu, X.; Li, F.; Chen, J. Rechargeable Aqueous Zinc-Manganese Dioxide Batteries with High Energy and Power Densities. *Nat. Commun.* **2017**, *8*, 405.
(38) Alfaruqi, M. H.; Gim, J.; Kim, S.; Song, J.; Pham, D. T.; Jo, J.; Xiu, Z.; Mathew, V.; Kim, J. A Layered δ-MnO_2 Nanoflake Cathode with High Zinc-Storage Capacities for Eco-Friendly Battery Applications. *Electrochem. Commun.* **2015**, *60*, 121−125.
(39) Sambandam, B.; Soundharrajan, V.; Kim, S.; Alfaruqi, M. H.; Jo, J.; Kim, S.; Mathew, V.; Sun, Y.-k.; Kim, J. Aqueous Rechargeable Zn-Ion Batteries: an Imperishable and High-Energy $Zn_2V_2O_7$ Nanowire Cathode through Intercalation Regulation. *J. Mater. Chem. A* **2018**, *6*, 3850−3856.
(40) Tang, B.; Fang, G.; Zhou, J.; Wang, L.; Lei, Y.; Wang, C.; Lin, T.; Tang, Y.; Liang, S. Potassium Vanadates with Stable Structure and Fast Ion Diffusion Channel as Cathode for Rechargeable Aqueous Zinc-ion Batteries. *Nano Energy* **2018**, *51*, 579−587.
(41) Li, G.; Yang, Z.; Jiang, Y.; Jin, C.; Huang, W.; Ding, X.; Huang, Y. Towards Polyvalent Ion Batteries: a Zinc-Ion Battery Based on NASICON Structured $Na_3V_2(PO_4)_3$. *Nano Energy* **2016**, *25*, 211−217.
(42) Li, W.; Wang, K.; Cheng, S.; Jiang, K. A Long-Life Aqueous Zn-Ion Battery Based on $Na_3V_2(PO_4)_2F_3$ Cathode. *Energy Storage Mater.* **2018**, *15*, 14−21.
(43) Zhang, L.; Chen, L.; Zhou, X.; Liu, Z. Towards High-Voltage Aqueous Metal-Ion Batteries Beyond 1.5 V: the Zinc/Zinc Hexacyanoferrate System. *Adv. Energy Mater.* **2015**, *5*, 1400930.
(44) Deiss, E. Spurious Chemical Diffusion Coefficients of Li^+ in Electrode Materials Evaluated with GITT. *Electrochim. Acta* **2005**, *50*, 2927−2932.
(45) He, P.; Quan, Y.; Xu, X.; Yan, M.; Yang, W.; An, Q.; He, L.; Mai, L. Q. High-Performance Aqueous Zinc-Ion Battery Based on Layered $H_2V_3O_8$ Nanowire Cathode. *Small* **2017**, *13*, 1702551.
(46) Ding, J.; Du, Z.; Gu, L.; Li, B.; Wang, L.; Wang, S.; Gong, Y.; Yang, S. Ultrafast Zn^{2+} Intercalation and Deintercalation in Vanadium Dioxide. *Adv. Mater.* **2018**, *30*, 1800762.
(47) Kim, H.-S.; Cook, J. B.; Lin, H.; Ko, J. S.; Tolbert, S. H.; Ozolins, V.; Dunn, B. Oxygen Vacancies Enhance Pseudocapacitive Charge Storage Properties of MoO_{3-x}. *Nat. Mater.* **2017**, *16*, 454−460.
(48) Zeng, Y.; Lai, Z.; Han, Y.; Zhang, H.; Xie, S.; Lu, X. Oxygen-Vacancy and Surface Modulation of Ultrathin Nickel Cobaltite Nanosheets as a High-Energy Cathode for Advanced Zn-Ion Batteries. *Adv. Mater.* **2018**, *30*, 1802396.
(49) Gan, Q.; He, H.; Zhao, K.; He, Z.; Liu, S.; Yang, S. Plasma-Induced Oxygen Vacancies in Urchin-Like Anatase Titania Coated by Carbon for Excellent Sodium-Ion Battery Anodes. *ACS Appl. Mater. Interfaces* **2018**, *10*, 7031−7042.
(50) Zhu, C.; Usiskin, R. E.; Yu, Y.; Maier, J. The Nanoscale Circuitry of Battery Electrodes. *Science* **2017**, *358*, No. eaao2808.
(51) Wang, X.; Wang, F.; Wang, L.; Li, M.; Wang, Y.; Chen, B.; Zhu, Y.; Fu, L.; Zha, L.; Zhang, L.; Wu, Y.; Huang, W. An Aqueous Rechargeable Zn//Co_3O_4 Battery with High Energy Density and Good Cycling Behavior. *Adv. Mater.* **2016**, *28*, 4904−4911.
(52) Ma, L.; Chen, S.; Pei, Z.; Li, H.; Wang, Z.; Liu, Z.; Tang, Z.; Zapien, J. A.; Zhi, C. Y. Flexible Waterproof Rechargeable Hybrid Zinc Batteries Initiated by Multifunctional Oxygen Vacancies-Rich Cobalt Oxide. *ACS Nano* **2018**, *12*, 8597−8505.

DOI: 10.1021/acsnano.9b04165
ACS Nano 2019, 13, 10376−10385